Available online at www.sciencedirect.com
SCIENCE DIRECT®
Journal of Computational Physics 188 (2003) 176–193
JOURNAL OF COMPUTATIONAL PHYSICS
www.elsevier.com/locate/jcp

Simulation of flows around an impulsively started circular cylinder by Taylor series expansion- and least squares-based lattice Boltzmann method

X.D. Niu, Y.T. Chew, C. Shu *

Department of Mechanical Engineering, National University of Singapore, Singapore 119260, Singapore

Received 26 July 2001; received in revised form 23 April 2002; accepted 21 February 2003

Abstract

The two-dimensional incompressible viscous flow past an impulsively started circular cylinder for a wide range of Reynolds numbers ($Re = 20$–9500) is studied computationally by using an explicit Taylor series expansion- and least squares-based lattice Boltzmann method. The final equation for distribution function in our method is in an explicit form and essentially has no limitation on choice of mesh structure and lattice model. It can be easily applied to simulation of flows with curved boundaries such as the problem considered in this work. For the flow past an impulsively started circular cylinder, numerical results obtained by present method agree very well with experimental data and computational results of Navier–Stokes equations available in the literature.
© 2003 Elsevier Science B.V. All rights reserved.

Keywords: Circular cylinder; Lattice Boltzmann equation; Explicit method; Taylor series expansion; Least square approach; Incompressible flow

1. Introduction

As a classical problem in fluid mechanics and a prototype of unsteady separated flows, the impulsively started cylinder problem has been the subject of many theoretical, experimental and computational works in the last century. Theoretical works of an impulsively started flow are generally based on the boundary-layer theory. Blasius [1] in 1908 first obtained a second order time series solution of this problem in the limiting case of infinite Reynolds number. Subsequently, many works have been carried out to attempt obtaining higher order solutions [2–6]. Among them, the most notable works are those of Collins and Dennis [4,5] based on the boundary layer equation and Bar-Lev and Yang [6] based on the vorticity equation. Both works provided extensive short-time information for flow quantities including vorticity field, streamlines and body forces.

* Corresponding author. Tel.: +65-874-6476; fax: +65-779-1459.
E-mail address: mpeshuc@nus.edu.sg (C. Shu).

0021-9991/03/$ - see front matter © 2003 Elsevier Science B.V. All rights reserved.
doi:10.1016/S0021-9991(03)00161-X

Many experimental investigations on unsteady flow around an impulsively started circular cylinder have been reported in the literature [7–11]. Among them, the works presented by Bouard and Coutanceau in 1980 seem to be the best. In their works, the phenomena of the formation and the development of the main and secondary vortices have been studied qualitatively and quantitatively in detail for Reynolds numbers up to 10^4.

Impulsively started flows present a serious challenge for numerical methods. Difficulties exist in the formulation of the boundary and initial conditions for the problem. Because the flow structure of this problem is complex and its development at early stage is very important to our understanding of the separation process, high-resolution simulations are necessary. The first computation of unsteady flow around an impulsively started cylinder was given in 1958 by Payen [12] for Reynolds numbers of 40 and 100. After that, numerous computations have been performed, and most of them are based on the vorticity-stream function formulation by using Eulerian, Lagrangian and hybrid methods for discretization. The most notable numerical works in recent years are those done by Loc [13], Loc and Bouard [14], Chang and Chern [15] and Koumoutsakos and Leonard [16]. Their works gave an extensive study of the wake length, separation angle, drag coefficient and vorticity distribution for Reynolds numbers up to 10^4. A high-resolution simulation with nearly complete and persuasive analysis of the underlying mechanism of unsteady separation has been presented by Koumoutsakos and Leonard [16].

It is indicated that all above numerical works are based on the macroscopic governing equations (Navier–Stokes equations), and numerical implementations have been becoming more and more complicated for obtaining high-resolution results. As an alternative computational fluid dynamics approach, the lattice Boltzmann method (LBM) has achieved a great success in fluid engineering in recent years [17–24]. Unlike the traditional CFD tools, which are based on the discretization of macroscopic continuum equations, the LBM is based on microscopic models and mesoscopic kinetic equations, and the macroscopic dynamics of a fluid is the result of the collective behavior of many microscopic particles in the system. The LBM has been proved to recover the Navier–Stokes equation by using the Chapman–Enskog expansion [25]. The major advantages of the LBM are its explicit feature of the governing equation-Lattice Boltzmann equation (LBE), easy for parallel computation, and simple implementation of boundary conditions on curved boundaries.

On the other hand, we should indicate that the standard LBE is restricted to the lattice-uniformity. So, it is usually applied on a uniform mesh in the Cartesian coordinate system, and cannot be directly applied to problems with complex geometry. Currently, there are two ways to improve the standard LBM so that it can be applied to complex problems. One is the interpolation-supplemented LBM (ISLBM) proposed by He and Doolen [19]. They successfully applied this approach to simulate flows past an impulsively started cylinder. The other is based on the solution of a differential lattice Boltzmann equation (LBE). For complex problems, the differential LBE can be solved by the finite difference (FDLBE) method with the help of coordinate transformation [20] or by the finite volume (FVLBE) approach [23]. Numerical experiences have shown that these methods have good capability in real applications. However, the ISLBE has an extra computational effort for interpolation at every time step, and it also has a strict restriction on selection of interpolation points. For the FDLBE and FVLBE methods, one needs to select efficient approaches such as upwind schemes to do numerical discretization in order to get the stable solution. As a consequence, the computational efficiency greatly depends on the selected numerical scheme.

In order to implement the LBE more efficiently for flows with complex geometry, Shu et al. [26] recently developed a new version of LBM, which is based the standard LBM, the well-known Taylor series expansion, the idea of developing Runge–Kutta method [27], and the least squares approach [28]. The final form of the method is an algebraic formulation, in which the coefficients only depend on the coordinates of mesh points and lattice velocity, and are computed in advance. The new method can also be applied to different lattice models. As shown in [26], for the driven cavity flow problem, the method can be easily applied to the uniform mesh and the non-uniform mesh. With the use of rectangular mesh, the method can

be applied to both the nine-velocity model and the seven-velocity model. Both velocity models provide the same numerical results but the seven-velocity model requires less computational effort. We also obtained very accurate results at $Re = 10^4$ with the use of non-uniform mesh. This shows that the numerical viscosity is well controlled in the new method. To further validate this method, the two-dimensional incompressible viscous flow past an impulsively started circular cylinder was simulated in this work for a wide range of Reynolds numbers ($Re = 20$–9500). The obtained numerical results are very accurate. They are compared well with available experimental data and numerical results of Navier–Stokes solvers.

2. Taylor series expansion- and least squares-based LBM

The method developed in this work is based on the fact that the distribution function is a continuous function in physical space and can be well defined for any mesh systems. Let us start with the standard LBM. The two dimensional, standard LBE with BGK approximation can be written as

$$f_\alpha(x + e_{\alpha x}\delta t, y + e_{\alpha y}\delta t, t + \delta t) = f_\alpha(x, y, t) + \frac{f_\alpha^{\mathrm{eq}}(x, y, t) - f_\alpha(x, y, t)}{\tau}, \quad \alpha = 0, 1, \ldots, N, \tag{1}$$

where τ is the single relaxation time; f_α is the density distribution function along the α direction; f_α^{eq} is its corresponding equilibrium state, which depends on the local macroscopic variables such as density ρ and velocity $\mathbf{U}(u, v)$; δt is the time step and $\mathbf{e}_\alpha(e_{\alpha x}, e_{\alpha y})$ is the particle velocity in the α direction; and N is the number of discrete particle velocities. Obviously, the standard LBE consists of two steps: collision and streaming. The macroscopic density ρ and momentum density $\rho\mathbf{U}$ are defined as

$$\rho = \sum_{\alpha=0}^{N} f_\alpha, \quad \rho\mathbf{U} = \sum_{\alpha=0}^{N} f_\alpha e_\alpha. \tag{2}$$

Suppose that a particle is initially at the grid point (x, y, t). Along the α direction, this particle will stream to the position $(x + e_{\alpha x}\delta t, y + e_{\alpha y}\delta t, t + \delta t)$. For a uniform lattice, $\delta x = e_{\alpha x}\delta_t$, $\delta y = e_{\alpha y}\delta_t$. So, $(x + e_{\alpha x}\delta t, y + e_{\alpha y}\delta t)$ is on the grid point. In other words, Eq. (1) can be used to update the density distribution functions exactly at the grid points. However, for a non-uniform grid, $(x + e_{\alpha x}\delta t, y + e_{\alpha y}\delta t)$ is usually not at the grid point $(x + \delta x, y + \delta y)$. In the numerical simulation, we are only interested in the density distribution function at the mesh point for all the time levels. So, the macroscopic properties such as the density, flow velocity can be evaluated at every mesh point. To get the density distribution function at the grid point $(x + \delta x, y + \delta y)$ and the time level $t + \delta t$, we need to apply the Taylor series expansion or other interpolation techniques such as the one used by He et al. [19]. In this work, the Taylor series expansion is used. Note that the time level for the position $(x + e_{\alpha x}\delta t, y + e_{\alpha y}\delta t)$ and the grid point $(x + \delta x, y + \delta y)$ is the same, that is, $t + \delta t$. So, the expansion in the time direction is not necessary. As shown in Fig. 1, we let point A represent the position (x_A, y_A), point A' represent the position $(x_A + e_{\alpha x}\delta t, y_A + e_{\alpha y}\delta t)$,

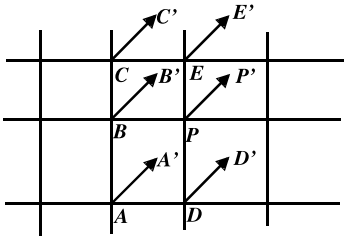

Fig. 1. Configuration of particle movement along the α direction.

and point P represent the position (x_P, y_P). Using Eq. (1), we can get the density distribution function at the position A' as

$$f_\alpha(A', t+\delta t) = f_\alpha(A,t) + [f_\alpha^{\mathrm{eq}}(A,t) - f_\alpha(A,t)]/\tau. \tag{3}$$

For the general case, A' may not coincide with the mesh point P. In the numerical simulation, we are only interested in the distribution function at the mesh point for all the time levels. So, the macroscopic properties such as the density, flow velocity can be evaluated at every mesh point. In this case, we need to obtain the density distribution function at the mesh point P. This can be done by applying the Taylor series expansion in the spatial direction only. With Taylor series expansion, $f_\alpha(A', t+\delta t)$ can be approximated by the corresponding function and its derivatives at the mesh point P as

$$\begin{aligned} f_\alpha(A', t+\delta t) = {} & f_\alpha(P, t+\delta t) + \Delta x_A \frac{\partial f_\alpha(P, t+\delta t)}{\partial x} + \Delta y_A \frac{\partial f_\alpha(P, t+\delta t)}{\partial y} + \frac{1}{2}(\Delta x_A)^2 \frac{\partial^2 f_\alpha(P, t+\delta t)}{\partial x^2} \\ & + \frac{1}{2}(\Delta y_A)^2 \frac{\partial^2 f_\alpha(P, t+\delta t)}{\partial y^2} + \Delta x_A \Delta y_A \frac{\partial^2 f_\alpha(P, t+\delta t)}{\partial x \partial y} + \mathrm{O}[(\Delta x_A)^3, (\Delta y_A)^3], \end{aligned} \tag{4}$$

where $\Delta x_A = x_A + e_{\alpha x}\delta t - x_P$, $\Delta y_A = y_A + e_{\alpha y}\delta t - y_P$. Note that the above approximation has a truncation error of the third order. Substituting Eq. (4) into Eq. (3) gives

$$\begin{aligned} & f_\alpha(P, t+\delta t) + \Delta x_A \frac{\partial f_\alpha(P, t+\delta t)}{\partial x} + \Delta y_A \frac{\partial f_\alpha(P, t+\delta t)}{\partial y} + \frac{1}{2}(\Delta x_A)^2 \frac{\partial^2 f_\alpha(P, t+\delta t)}{\partial x^2} \\ & + \frac{1}{2}(\Delta y_A)^2 \frac{\partial^2 f_\alpha(P, t+\delta t)}{\partial y^2} + \Delta x_A \Delta y_A \frac{\partial^2 f_\alpha(P, t+\delta t)}{\partial x \partial y} = f_\alpha(A,t) + [f_\alpha^{\mathrm{eq}}(A,t) - f_\alpha(A,t)]/\tau. \end{aligned} \tag{5}$$

It is indicated that Eq. (5) is a differential equation, which only involves two mesh points A and P. Solving Eq. (5) can provide the density distribution functions at all the mesh points. Eq. (5) can be considered as a new version of differential LBE, which can give very accurate numerical results. In this work, we go further to develop a new solution procedure. In fact, our new development is inspired from the Runge–Kutta method. As we know, the Runge–Kutta method is developed to improve the Taylor series method in the solution of ordinary differential equations (ODEs). Like Eq. (5), Taylor series method involves evaluation of different orders of derivatives to update the functional value at the next time level. For a complicated expression of given ODEs, this application is very difficult. To improve the Taylor series method, the Runge—Kutta method evaluates the functional values at some intermediate points and then combines them (through the Taylor series expansion) to form a scheme with the same order of accuracy. With this idea in mind, we look at Eq. (5). We know that at the time level $t+\delta t$, the density distribution function and its derivatives at the mesh point P are all unknowns. So, Eq. (5) has six unknowns in total. To solve for the six unknowns, we need six equations. However, Eq. (5) just provides one equation. We need additional five equations to close the system. As shown in Fig. 1, we can see that along the α direction, the particles at five mesh points P, B, C, D, E at the time level t will move to the new positions P', B', C', D', E' at the time level $t+\delta t$. The density distribution functions at these new positions can be computed through Eq. (1), which are given below

$$f_\alpha(P', t+\delta t) = f_\alpha(P,t) + [f_\alpha^{\mathrm{eq}}(P,t) - f_\alpha(P,t)]/\tau, \tag{6}$$

$$f_\alpha(B', t+\delta t) = f_\alpha(B,t) + [f_\alpha^{\mathrm{eq}}(B,t) - f_\alpha(B,t)]/\tau, \tag{7}$$

$$f_\alpha(C', t+\delta t) = f_\alpha(C,t) + [f_\alpha^{\mathrm{eq}}(C,t) - f_\alpha(C,t)]/\tau, \tag{8}$$

$$f_\alpha(D',t+\delta t) = f_\alpha(D,t) + [f_\alpha^{\mathrm{eq}}(D,t) - f_\alpha(D,t)]/\tau, \tag{9}$$

$$f_\alpha(E',t+\delta t) = f_\alpha(E,t) + [f_\alpha^{\mathrm{eq}}(E,t) - f_\alpha(E,t)]/\tau. \tag{10}$$

Using Taylor series expansion, $f_\alpha(P',t+\delta t)$, $f_\alpha(B',t+\delta t)$, $f_\alpha(C',t+\delta t)$, $f_\alpha(D',t+\delta t)$, $f_\alpha(E',t+\delta t)$ in above equations can be approximated by the function and its derivatives at the mesh point P. As a result, Eqs. (6)–(10) can be reduced to

$$\begin{aligned} &f_\alpha(P,t+\delta t) + \Delta x_P \frac{\partial f_\alpha(P,t+\delta t)}{\partial x} + \Delta y_P \frac{\partial f_\alpha(P,t+\delta t)}{\partial y} + \frac{1}{2}(\Delta x_P)^2 \frac{\partial^2 f_\alpha(P,t+\delta t)}{\partial x^2} \\ &\quad + \frac{1}{2}(\Delta y_P)^2 \frac{\partial^2 f_\alpha(P,t+\delta t)}{\partial y^2} + \Delta x_P \Delta y_P \frac{\partial^2 f_\alpha(P,t+\delta t)}{\partial x \partial y} = f_\alpha(P,t) + \left[f_\alpha^{\mathrm{eq}}(P,t) - f_\alpha(P,t)\right]/\tau, \end{aligned} \tag{11}$$

$$\begin{aligned} &f_\alpha(P,t+\delta t) + \Delta x_B \frac{\partial f_\alpha(P,t+\delta t)}{\partial x} + \Delta y_B \frac{\partial f_\alpha(P,t+\delta t)}{\partial y} + \frac{1}{2}(\Delta x_B)^2 \frac{\partial^2 f_\alpha(P,t+\delta t)}{\partial x^2} \\ &\quad + \frac{1}{2}(\Delta y_B)^2 \frac{\partial^2 f_\alpha(P,t+\delta t)}{\partial y^2} + \Delta x_B \Delta y_B \frac{\partial^2 f_\alpha(P,t+\delta t)}{\partial x \partial y} = f_\alpha(B,t) + \left[f_\alpha^{\mathrm{eq}}(B,t) - f_\alpha(B,t)\right]/\tau, \end{aligned} \tag{12}$$

$$\begin{aligned} &f_\alpha(P,t+\delta t) + \Delta x_C \frac{\partial f_\alpha(P,t+\delta t)}{\partial x} + \Delta y_C \frac{\partial f_\alpha(P,t+\delta t)}{\partial y} + \frac{1}{2}(\Delta x_C)^2 \frac{\partial^2 f_\alpha(P,t+\delta t)}{\partial x^2} \\ &\quad + \frac{1}{2}(\Delta y_C)^2 \frac{\partial^2 f_\alpha(P,t+\delta t)}{\partial y^2} + \Delta x_C \Delta y_C \frac{\partial^2 f_\alpha(P,t+\delta t)}{\partial x \partial y} = f_\alpha(C,t) + \left[f_\alpha^{\mathrm{eq}}(C,t) - f_\alpha(C,t)\right]/\tau, \end{aligned} \tag{13}$$

$$\begin{aligned} &f_\alpha(P,t+\delta t) + \Delta x_D \frac{\partial f_\alpha(P,t+\delta t)}{\partial x} + \Delta y_D \frac{\partial f_\alpha(P,t+\delta t)}{\partial y} + \frac{1}{2}(\Delta x_D)^2 \frac{\partial^2 f_\alpha(P,t+\delta t)}{\partial x^2} \\ &\quad + \frac{1}{2}(\Delta y_D)^2 \frac{\partial^2 f_\alpha(P,t+\delta t)}{\partial y^2} + \Delta x_D \Delta y_D \frac{\partial^2 f_\alpha(P,t+\delta t)}{\partial x \partial y} = f_\alpha(D,t) + \left[f_\alpha^{\mathrm{eq}}(D,t) - f_\alpha(D,t)\right]/\tau, \end{aligned} \tag{14}$$

$$\begin{aligned} &f_\alpha(P,t+\delta t) + \Delta x_E \frac{\partial f_\alpha(P,t+\delta t)}{\partial x} + \Delta y_E \frac{\partial f_\alpha(P,t+\delta t)}{\partial y} + \frac{1}{2}(\Delta x_E)^2 \frac{\partial^2 f_\alpha(P,t+\delta t)}{\partial x^2} \\ &\quad + \frac{1}{2}(\Delta y_E)^2 \frac{\partial^2 f_\alpha(P,t+\delta t)}{\partial y^2} + \Delta x_E \Delta y_E \frac{\partial^2 f_\alpha(P,t+\delta t)}{\partial x \partial y} = f_\alpha(E,t) + \left[f_\alpha^{\mathrm{eq}}(E,t) - f_\alpha(E,t)\right]/\tau, \end{aligned} \tag{15}$$

where

$$\Delta x_P = e_{\alpha x}\delta t, \quad \Delta y_P = e_{\alpha y}\delta t,$$

$$\Delta x_B = x_B + e_{\alpha x}\delta t - x_P, \quad \Delta y_B = y_B + e_{\alpha y}\delta t - y_P,$$

$$\Delta x_C = x_C + e_{\alpha x}\delta t - x_P, \quad \Delta y_C = y_C + e_{\alpha y}\delta t - y_P,$$

$$\Delta x_D = x_D + e_{\alpha x}\delta t - x_P, \quad \Delta y_D = y_D + e_{\alpha y}\delta t - y_P,$$

$$\Delta x_E = x_E + e_{\alpha x}\delta t - x_P, \quad \Delta y_E = y_E + e_{\alpha y}\delta t - y_P.$$

Eqs. (5), (11)–(15) form a system to solve for six unknowns. Now, we define

$$g_i = f_\alpha(x_i, y_i, t) + \left[f_\alpha^{\mathrm{eq}}(x_i, y_i, t) - f_\alpha(x_i, y_i, t)\right]/\tau, \tag{16}$$

$$\{s_i\}^{\mathrm{T}} = \{1, \Delta x_i, \Delta y_i, (\Delta x_i)^2/2, (\Delta y_i)^2/2, \Delta x_i \Delta y_i\}, \tag{17}$$

$$\{V\} = \{f_\alpha, \partial f_\alpha/\partial x, \partial f_\alpha/\partial y, \partial^2 f_\alpha/\partial x^2, \partial^2 f_\alpha/\partial^2 y, \partial^2 f_\alpha/\partial x \partial y\}^{\mathrm{T}}, \tag{18}$$

where g_i is the post-collision state of the distribution function at the ith point and the time level t, $\{s_i\}^{\mathrm{T}}$ is a vector with 6 elements formed by the coordinates of mesh points, $\{V\}$ is the vector of unknowns at the mesh point P, which also has 6 elements. Our target is to find its first element $V_1 = f_\alpha(P, t + \delta t)$. With above definitions, Eqs. (5), (11)–(15) can be written as

$$g_i = \{s_i\}^{\mathrm{T}}\{V\} = \sum_{j=1}^{6} s_{i,j} V_j, \quad i = P, A, B, C, D, E, \tag{19}$$

where $s_{i,j}$ is the jth element of the vector $\{s_i\}^{\mathrm{T}}$ and V_j is the jth element of the vector {V}. Equation system (19) can be put into the following matrix form

$$[S]\{V\} = \{g\}, \tag{20}$$

where $\{g\} = \{g_P, g_A, g_B, g_C, g_D, g_E\}^{\mathrm{T}}$

$$[S] = [s_{i,j}] = \begin{bmatrix} \{s_P\}^{\mathrm{T}} \\ \{s_A\}^{\mathrm{T}} \\ \{s_B\}^{\mathrm{T}} \\ \{s_C\}^{\mathrm{T}} \\ \{s_D\}^{\mathrm{T}} \\ \{s_E\}^{\mathrm{T}} \end{bmatrix} = \begin{bmatrix} 1 & \Delta x_P & \Delta y_P & (\Delta x_P)^2/2 & (\Delta y_P)^2/2 & \Delta x_P \Delta y_P \\ 1 & \Delta x_A & \Delta y_A & (\Delta x_A)^2/2 & (\Delta y_A)^2/2 & \Delta x_A \Delta y_A \\ 1 & \Delta x_B & \Delta y_B & (\Delta x_B)^2/2 & (\Delta y_B)^2/2 & \Delta x_B \Delta y_B \\ 1 & \Delta x_C & \Delta y_C & (\Delta x_C)^2/2 & (\Delta y_C)^2/2 & \Delta x_C \Delta y_C \\ 1 & \Delta x_D & \Delta y_D & (\Delta x_D)^2/2 & (\Delta y_D)^2/2 & \Delta x_D \Delta y_D \\ 1 & \Delta x_E & \Delta y_E & (\Delta x_E)^2/2 & (\Delta y_E)^2/2 & \Delta x_E \Delta y_E \end{bmatrix}.$$

Note that the matrix $[S]$ only depends on the coordinates of mesh points, which can be computed once and stored for the application of Eq. (20) at all time levels. In practical applications, it was found that the matrix $[S]$ might be singular or ill-conditioned. To overcome this difficulty and make the method be more general, we propose the following least squares-based LBM.

Eq. (19) has six unknowns (elements of the vector $\{V\}$). If Eq. (19) is applied at more than 6 mesh points, then the system is over-determined. For this case, the unknown vector can be decided from the least square method. For simplicity, let the mesh point P be represented by the index $i = 0$, and its adjacent points be represented by index $i = 1, 2, \ldots, M$, where M is the number of neighbouring points around P and it should be larger than 5. At each point, we can define an error in terms of Eq. (19), that is,

$$\mathrm{err}_i = g_i - \sum_{j=1}^{6} s_{i,j} V_j, \quad i = 0, 1, 2, \ldots, M. \tag{21}$$

The square sum of all the errors are defined as

$$E = \sum_{i=0}^{M} \mathrm{err}_i^2 = \sum_{i=0}^{M} \left(g_i - \sum_{j=1}^{6} s_{i,j} V_j \right)^2. \tag{22}$$

To minimize the error E, we need to set $\partial E/\partial V_k = 0, k = 1, 2, \ldots, 6$, which leads to

$$[S]^{\mathrm{T}}[S]\{V\} = [S]^{\mathrm{T}}\{g\}, \tag{23}$$

where $[S]$ is a $(M+1)\times 6$ dimensional matrix, which is given as

$$[S] = \begin{bmatrix} 1 & \Delta x_0 & \Delta y_0 & (\Delta x_0)^2/2 & (\Delta y_0)^2/2 & \Delta x_0 \Delta y_0 \\ 1 & \Delta x_1 & \Delta y_1 & (\Delta x_1)^2/2 & (\Delta y_1)^2/2 & \Delta x_1 \Delta y_1 \\ - & - & - & - & - & - \\ - & - & - & - & - & - \\ - & - & - & - & - & - \\ 1 & \Delta x_M & \Delta y_M & (\Delta x_M)^2/2 & (\Delta y_M)^2/2 & \Delta x_M \Delta y_M \end{bmatrix}_{(M+1)\times 6}$$

and $\{g\} = \{g_0, g_1, \ldots, g_M\}^{\mathrm{T}}$.

The Δx and Δy values in the matrix $[S]$ are given as

$$\Delta x_0 = e_{\alpha x}\delta t, \Delta y_0 = e_{\alpha y}\delta t, \tag{24a}$$

$$\Delta x_i = x_i + e_{\alpha x}\delta t - x_0, \Delta y_i = y_i + e_{\alpha y}\delta t - y_0 \quad \text{for } i = 1, 2, \ldots, M. \tag{24b}$$

Clearly, when the coordinates of mesh points are given, and the particle velocity and time step size are specified, the matrix $[S]$ is determined. Then from Eq. (23), we obtain

$$\{V\} = ([S]^{\mathrm{T}}[S])^{-1}[S]^{\mathrm{T}}\{g\} = [A]\{g\}. \tag{25}$$

Note that $[A]$ is a $6\times(M+1)$ dimensional matrix. From Eq. (25), we can have

$$f_\alpha(x_0, y_0, t+\delta t) = V_1 = \sum_{k=1}^{M+1} a_{1,k} g_{k-1}, \tag{26}$$

where $a_{1,k}$ are the elements of the first row of the matrix $[A]$, which are pre-computed before the LBM is applied. Therefore, little computational effort is introduced as compared with the standard LBE. Note that our method is actually a kind of interpolation methods, but the interpolation coefficients are built in the formulation (26). So, we just need to compute these coefficients once, store them for the use in all the time levels.

3. D2Q7 lattice model and implementation of boundary conditions

It can be seen that Eq. (26) is applied along the α direction. Here α can be any direction. This implies that Eq. (26) can be uniformly applied to the different lattice models. As shown in [26], D2Q7 and D2Q9 can provide the same results on the rectangular mesh, but D2Q7 requires less computational effort. So, in this work, we select the D2Q7 model. The configuration of this model is shown in Fig. 2. The discrete velocity of this model is defined as

$$\mathbf{e}_\alpha = \begin{cases} (0,0), & \alpha = 0, \\ (\cos[(\alpha-1)\pi/3], \sin[(\alpha-1)\pi/3])c, & \alpha = 1, 2, \ldots, 6. \end{cases} \tag{27}$$

The parameter c is the particle streaming speed. The fluid kinetic viscosity is given by

$$\upsilon = \frac{(2\tau-1)}{8}c^2\delta t \tag{28}$$

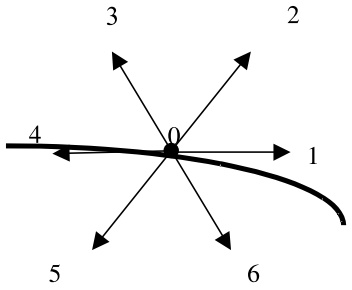

Fig. 2. Schematic plot of D2Q7 model on a solid boundary (thick black line).

and the equilibrium density distribution f_α^{eq} is chosen to be

$$f_\alpha^{\mathrm{eq}} = \rho\left[\frac{1}{2}+\frac{1}{6}\left(2\frac{\mathbf{e}_\alpha\cdot\mathbf{U}}{c^2}+4\left(\frac{\mathbf{e}_\alpha\cdot\mathbf{U}}{c^2}\right)^2-\frac{\mathbf{U}^2}{c^2}\right)\right]. \tag{29}$$

The speed of sound of this model is $c_s = c/2$, and the equation of state is $P = \rho c_s^2$ for an ideal gas. Although the proposed method has meshless feature, it is recommended to use a structured grid. This is because in our method, only the coordinates of mesh points are involved. When a structured grid is used, it is much easy for us to define the coordinates of mesh points. In our application, we use a structured grid, and take M as 8 for convenience. As shown in Fig. 3, for an internal mesh point (i,j) (noted as "0" in Eq. (26)), the 8 neighbouring points are taken as $(i-1,j-1)$; $(i-1,j)$; $(i-1,j+1)$; $(i,j-1)$; $(i,j+1)$, $(i+1,j-1)$; $(i+1,j)$; $(i+1,j+1)$. Therefore, at each mesh point, we only need to store 9 coefficients $a_{1,k}$, $k = 1,2,\ldots,9$ before Eq. (26) is applied. Note that the configuration of 9 mesh points as shown in Fig. 3 is applied in all lattice directions ($\alpha = 1,2,\ldots,6$).

Implementation of boundary conditions is an essiential issue in LBM. In this work, we found that a complete half-way wall bounceback condition [22] is the most simple and efficent method in treating the circular cylinder wall, where the non-slip condition holds. The complete half-way wall bounceback condition, which originated from LGCA, assigns each f_α the value of the f_α in its opposite direction with no relaxation on the bounceback points. The treament is independent of the direction, which gives us more conveniences in treating complicated boundary problems. The complete half-way wall bounceback condition has second order of accuaracy because macroscopic quantities such as stress force is evaluated on the half-way wall between the bounceback row and the first flow row. As shown in Fig. 2, for the D2Q7 model, at a boundary point, f_1, f_2 and f_3 point to the flow field from the wall, which will be determined from the boundary condition. f_4, f_5, f_6 are computed by streaming from points inside the flow field. So, using the half-way wall bounceback condition, f_1, f_2 and f_3 are evaluated as

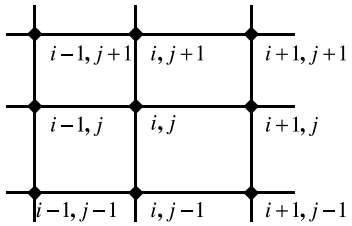

Fig. 3. Schematic plot of neighboring point distributions around the point (i,j).

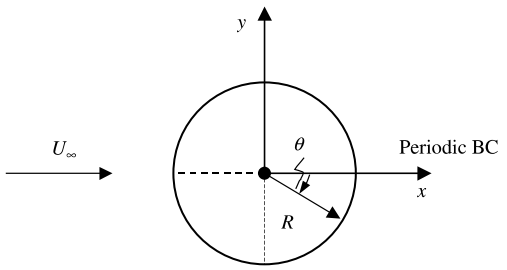

Fig. 4. A sketch of the flow past an impulsively started circular cylinder.

$$f_1 = f_4, \quad f_2 = f_5, \quad f_3 = f_6. \tag{30}$$

On the far field boundary, it is reasonable to assume that the flow is a potential one with the density distribution function at its equilibrium state. Periodic boundary condition is applied on the cut line, which starts from the rear point of the cylinder wall and is along the positive x axis. In our computation, an irrotational, potential flow field is taken as the initial condition. The upstream velocity U_∞ and density ρ_∞ are set to be 0.15 and 1.0, respectively. A typical sketch of this problem is shown in Fig. 4.

4. Simulation of flows around an impulsively started circular cylinder

The impulsively started cylinder problem has been considered as a good prototype of unsteady separated flows. The present method was developed from the application of Taylor series expansion only in the spatial directions. The time accuracy of present method is kept the same as the standard LBE. So, the simulation of steady and unsteady flows around an impulsively started circular cylinder at the early stage is a good test case for validation of our new method. In this work, the Reynolds number ($Re = U_\infty D/\upsilon$), based on the upstream velocity U_∞ and the diameter of the cylinder D, is selected to be 20, 40, 550, 3000 and 9500, respectively.

4.1. Flows at $Re = 20$ and 40

At these two low Reynolds numbers, it is well known that the flow will eventually develop into a steady state. In our simulations, unless otherwise mentioned, the far field boundary is set at 50.5 diameters away from the center of the cylinder and a 241 × 181 O-type grid is used (a typical mesh is shown in Fig. 5). With

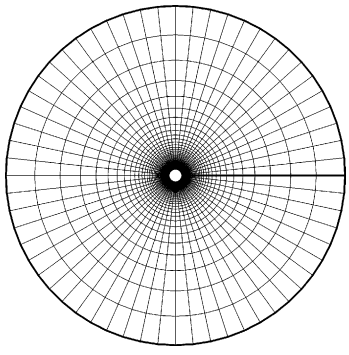

Fig. 5. Computational mesh for flow around a circular cylinder.

this grid distribution, the time step, in units of $D/(2U_\infty)$, is equal to 0.00375, and the maximum grid stretch ratio $r_{\max}$ (defined as the ratio of the maximum mesh spacing over the minimum mesh spacing) is 160.7.

Figs. 6–8 show the time evolution of the wake length L, separation angle θ_s and drag coefficient C_d at Reynolds numbers of 20 and 40, where C_d is defined as $C_d = 2\mathbf{F}\cdot\mathbf{X}/(\rho U^2 D)$ and $\mathbf{F} = \int[-pI + \rho\upsilon(\nabla\mathbf{U} + \mathbf{U}\nabla)]\cdot\mathbf{n}dl\cdot\mathbf{n}$ is the normal vector of the cylinder surface. To test the accuracy of numerical results obtained by the present method, experimental data given by Coutanceau and Bouard [9,10] are also shown in Figs. 6 and 7 for comparison. Due to the lack of experimental data, only the numerical results of Navier–Stokes equations for C_d at Reynolds number of 40 given by Koumoutsakos and Leonard

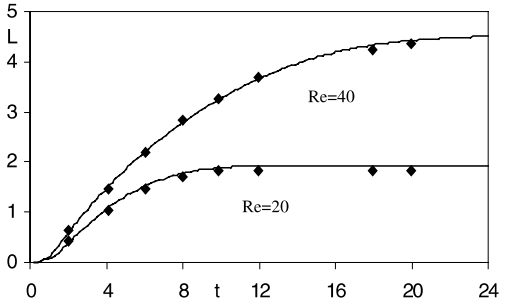

Fig. 6. Time evolution of the wake length for different Reynolds numbers (◆, experimental data by Coutanceu and Bouard [10]; –, present results).

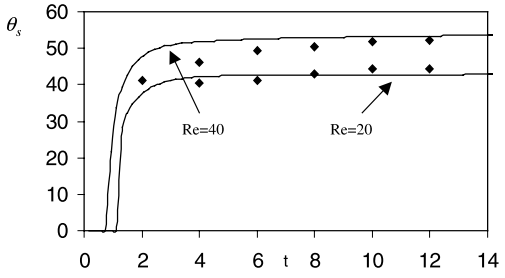

Fig. 7. Time evolution of the separation angle for different Reynolds numbers (◆, experimental data by Coutanceu and Bouard [10]; –, present results).

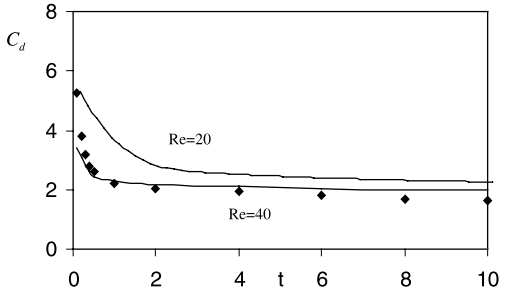

Fig. 8. Time evolution of the drag coefficient for different Reynolds numbers (◆, numerical results of Koumoutsakos and Leonard [16]; –, present results).

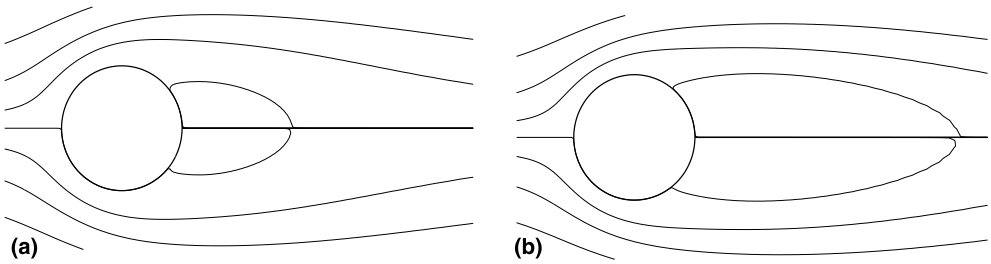

Fig. 9. Streamlines at the final steady state for different Reynolds numbers. (a) $Re = 20$, (b) $Re = 40$.

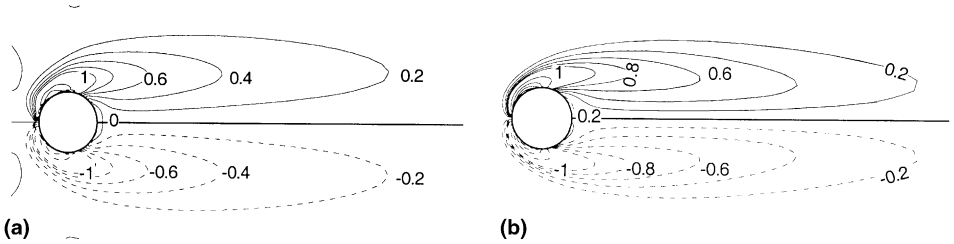

Fig. 10. Vorticity contours at the final steady state for different Reynolds numbers. (a) $Re = 20$, (b) $Re = 40$.

[16] are shown in Fig. 8 for comparison. The wake length and time are expressed in units of $D/2$ and $D/(2U_\infty)$, respectively. From these three figures, we can see that the results obtained by the present method generally agree well with experimental data and numerical results of Navier–Stokes equations except that the separation angle at $Re = 40$ has a little faster development than the experimental results.

Table 1
Comparisons of geometrical and dynamic parameters with previous studies

		Reynolds number	
		20	40
L	Ref. [29]	1.88	4.69
	Ref. [19]	1.842	4.49
	Present method	1.92	4.51
θ_s (degree)	Ref. [29]	43.7	53.8
	Ref. [19]	42.96	52.84
	Present method	42.79	53.8
C_d	Ref. [29]	2.045	1.522
	Ref. [19]	2.152	1.499
	Present method	2.111	1.574
C_p (front)	Ref. [29]	1.269	1.114
	Ref. [19]	1.233	1.133
	Present method	1.230	1.147
C_p (rear)	Ref. [29]	−0.589	−0.509
	Ref. [19]	−0.567	−0.487
	Present method	−0.614	−0.555

Figs. 9 and 10 show the streamlines and vorticity contours in the final steady state of our simulations, respectively. As shown in Fig. 9, a pair of symmetric vortices is developed behind the cylinder at these two Reynolds numbers. We also see that the secondary vortices have formed and remain unchanged as they are confined by the primary vortices (see Fig. 10). The quantitative comparisons of the wake length, separation angle, drag coefficient and pressure coefficients C_p at the front and rear stagnation points with previous studies [19,29] are listed in Table 1. The pressure coefficient is defined as $C_p = 2(p - p_\infty)/(\rho U^2)$. Obviously, good agreements are achieved between the results of our simulation and those of the previous studies.

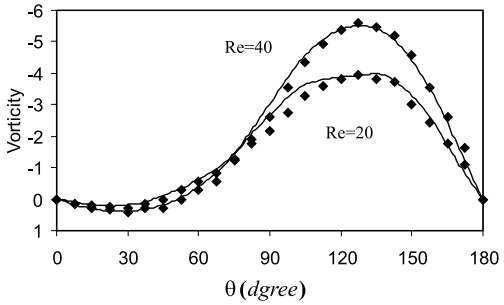

Fig. 11. Vorticity distributions over the cylinder surface at different Reynolds numbers (◆, results of Fornberg [30]; –, present results).

Table 2
Effect of mesh size on wake length, separation angle and drag coefficient

	Grid number		
	181 × 121	241 × 181	301 × 241
$Re = 20$			
L	1.943	1.92	1.90
θ_s (degree)	42.73	42.79	42.26
C_d	2.111	2.111	2.122
$Re = 40$			
L	4.478	4.51	4.502
θ_s (degree)	53.82	53.8	53.59
C_d	1.572	1.574	1.577

Table 3
Effect of far field boundary on wake length, separation angle and drag coefficient

	Location of outer boundary		
	25.5D	50.5D	75.5D
$Re = 20$			
L	1.902	1.92	1.930
θ_s (degree)	45.48	42.79	42.87
C_d	2.056	2.111	2.099
$Re = 40$			
L	4.17	4.51	4.56
θ_s (degree)	55.42	53.8	53.89
C_d	1.557	1.574	1.565

The vorticity distributions over the cylinder surface are displayed in Fig. 11. The numerical results of Fernberg [30] by solving Navier–Stokes equations are also shown in this figure for comparison. Again, good agreement is obtained between the present results and Navier–Stokes solutions.

We also studied the effects of grid sensitivity and location of the outer boundary at these two Reynolds numbers. The detailed results for this study are listed in Tables 2 and 3, respectively. As shown in Table 2, the grid size of 241×181 is fine enough to obtain accurate numerical results. Table 3 shows that as the outer boundary moves from $25.5D$ to $75.5D$, the drag coefficient varies between 6%, the wake length increases by 6% and the separation angle changes about 5%. This means that the effect of outer boundary is not critical if it is above $25.5D$.

4.2. Flows at $Re = 550$, 3000 and 9500

The flow around an impulsively started circular cylinder at these three Reynolds numbers is known to develop eventually the three-dimensional phenomenon. However, careful flow visualization reveals that the flow in the early stage of development in the laminar wake region is still two-dimensional. In the present study, we only focus on the early stage of flow development.

For Reynolds numbers of 550 and 3000, the outer boundary is placed at 15.5 diameters away from the center of the cylinder, the grid size is taken as 241×121 with the maximum grid stretch ratio of $r_{\max} = 159$, and the time step, in units of $D/(2U_\infty)$, is equal to 0.001875. For the Reynolds number of 9500, the corresponding parameters are taken as 3, 241×301 with $r_{\max} = 6.7$ and $\Delta t = 0.00075$, respectively.

Figs. 12–14 give the time evolution of the streamlines and vorticity contours at different Reynolds numbers. For Reynolds numbers of 550 (Fig. 12) and 3000 (Fig. 13), both cases show that a pair of primary

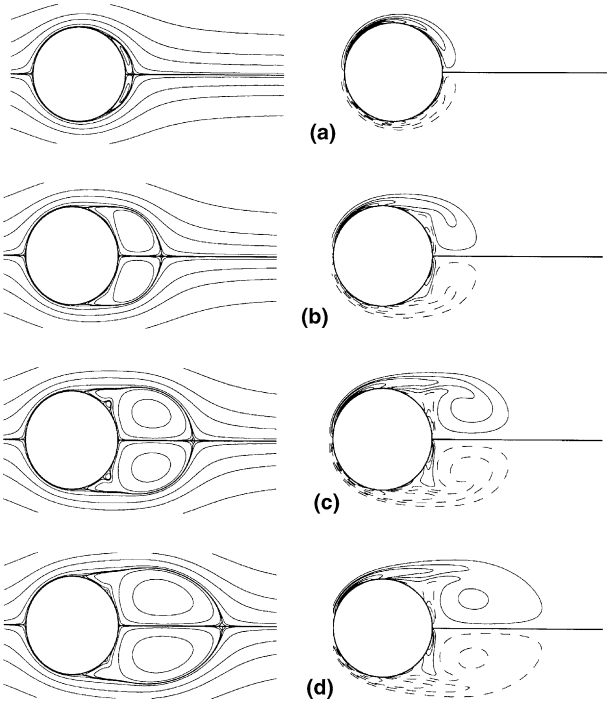

Fig. 12. Instantaneous streamlines (left) and vorticity contours (right) at $Re = 550$ (dash line represents the negative vorticity). (a) $t = 1$, (b) $t = 3$, (c) $t = 5$, and (d) $t = 7$.

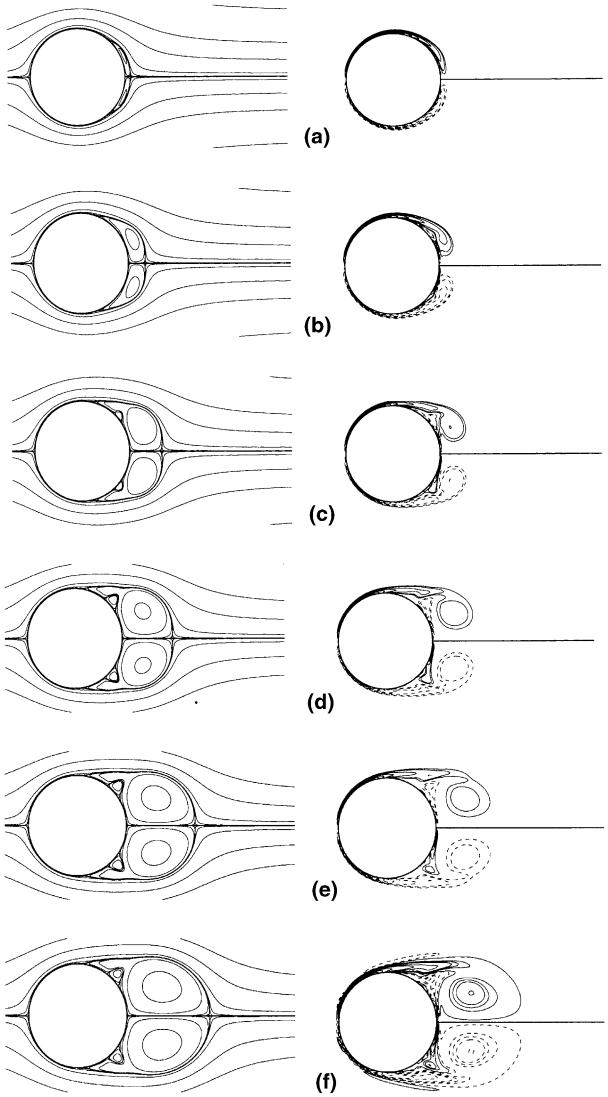

Fig. 13. Instantaneous streamlines (left) and vorticity contours (right) at $Re = 3000$ (dash line represents the negative vorticity). (a) $t = 1$, (b) $t = 2$, (c) $t = 3$, (d) $t = 4$, (e) $t = 5$, and (f) $t = 6$.

symmetric vortices has been formed at the rear of the cylinder by $t = 1.0$ and that their vorticity strengths increase with the Reynolds number. As time increases, a pair of secondary symmetric vortices appears and becomes stronger and stronger. However, it is confined by the primary vortices and cannot reaches to the outer irrotational flow field. The layer that initially feeds the secondary vortices changes angle of orientation in respect to the cylinder surface but it seems to remain a stable configuration beyond $t = 5.0$. This is the so-called α-phenomena observed experimentally by Bouard et al. [11]. For flow at Reynolds number of 9500 (Fig. 14), the so-called β-phenomena observed in [11] is also captured by our simulation. Initially a stable configuration of a very thin layer of vorticity (''forewake'' in [11]) is formed before $t = 1.0$. The core of the vortex gradually separates into two parts, one forms a secondary vortex ($t = 2.0$) and the other is absorbed into the primary vortex. As the secondary vortex becomes stronger, it rises rapidly, penetrates the

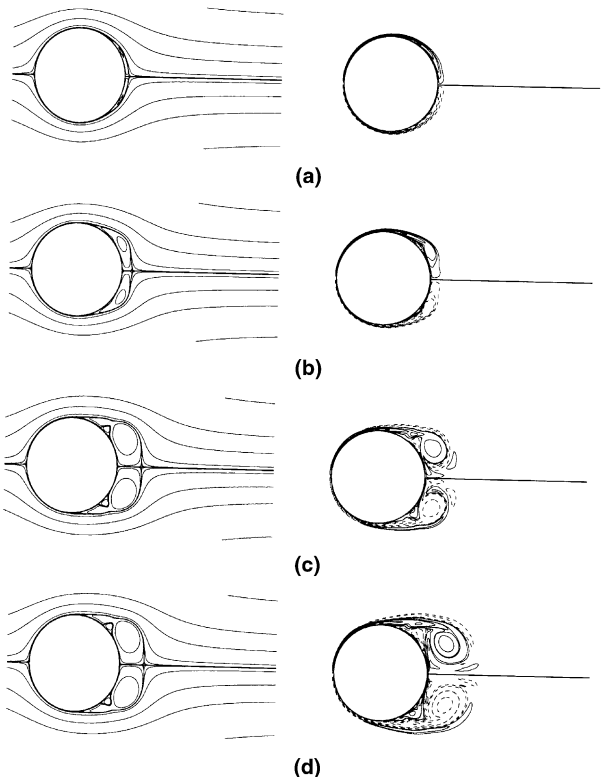

Fig. 14. Instantaneous streamlines (left) and vorticity contours (right) at $Re = 9500$ (dash line represents the negative vorticity). (a) $t = 1$, (b) $t = 2$, (c) $t = 3$, and (d) $t = 4$.

primary vortex and reaches the outer flow at $t = 3$. The primary vortex then rolls up and eventually detaches from the cylinder surface. This makes the strength of the secondary vortex reduce and a new vortex forms. As the new vortex moves downstream, it gradually merges with the primary vortex, re-establishing the link between the cylinder surface and the primary vortex ($t = 4.0$). From these three figures, we can see that the flow patterns in our simulation match well with the experimental and numerical findings given in [11,13,14,16,19].

The time histories of vorticity distribution on the surface of the cylinder at different Reynolds numbers are shown in Fig. 15. It is seen that the vorticity on the cylinder surface has a tendency to be stationary as time increases, and seems to become stronger as Reynolds number is increased. For Reynolds number of 550, a tertiary vortical region is observed at about $\pm 45°$ from the rear stagnation point at $t = 3$ (Fig. 15(a)); For Reynolds number of 3000, the strongest secondary vortex is formed at about $\pm 30°$ from the rear of the cylinder at $t = 2.0$. This secondary vortex induces in turn tertiary vortical regions of the cylinder surface (Fig. 15(b)). As shown in Fig. 15(c), when flow at Reynolds number of 9500 develops beyond $t = 2$, a series of tertiary vortical phenomena appears on the surface of the cylinder and the unsteady separation procedure at smaller scales repetitively occurs. The results shown in these figures agree well with the results of Koumoutsakos and Leonard [16], Loc and Bourd [14], and Chang and Chern [15] by solving Navier–Stokes equations.

The radial velocity profiles obtained by present method on the symmetric axis in the near wake for $Re = 3000$ and 9500 and at different times are compared with those of Bouard and Coutanceau [11] in Fig. 16. For $Re = 3000$, the agreement is very good up to $t = 3$. There is a little discrepancy between the two results at $t = 5$. For the case of $Re = 9500$, the present results have a little difference from those of Bouard

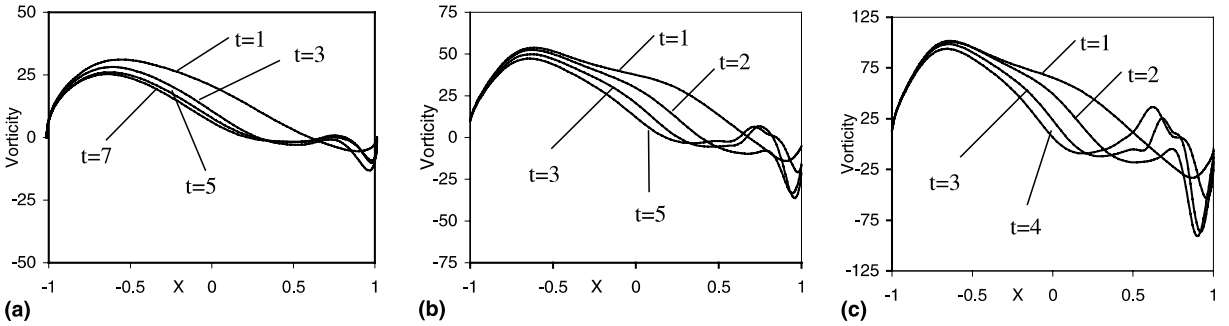

Fig. 15. Instantaneous vorticity distributions on the cylinder surface at different Reynolds numbers. (a) $Re = 550$, (b) $Re = 3000$, and (c) $Re = 9500$.

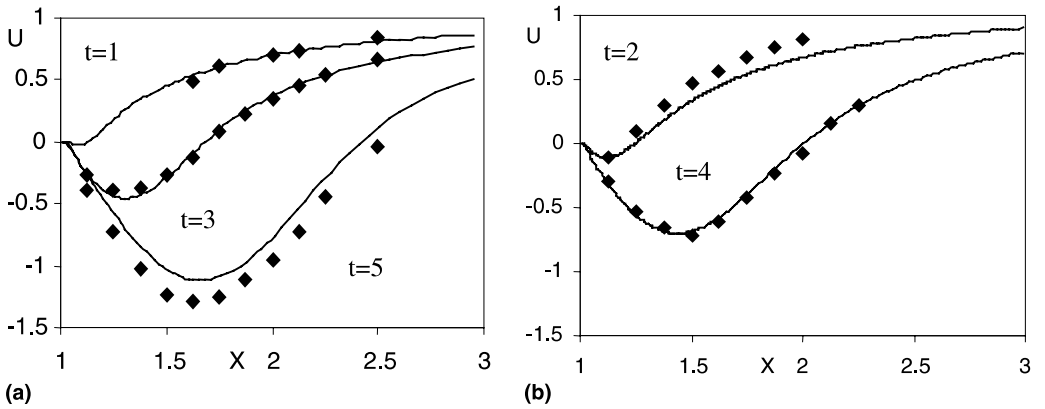

Fig. 16. Radial velocity profiles on the symmetric axis behind the cylinder for $Re = 3000$ and 9500 at different times (◆, experimental data of Bouard and Coutanceau [11]; –, present results). (a) $Re = 3000$, (b) $Re = 9500$.

and Coutanceau [11] at $t = 2$. But at $t = 4$, both results agree very well. It can be seen that the recirculation is the strongest in the middle wake along the symmetric axis.

Figs. 17 and 18 show a quantitative comparison for the time evolution of the wake length and drag coefficient between the present results and the experimental data [14] as well as the numerical results of Navier–Stokes solvers [15]. Obviously, good agreement is achieved between our simulation and the previous works. The wake length increases linearly with time for $Re = 550$. For Reynolds numbers of 3000 and 9500, the wake length has a slow growth at beginning and a fast development after $t = 3$. These two stages reflect the formation and destruction of the " forewake". The development of the flow field is also manifested in the drag curves. From Fig. 18, one can easily observe that all curves have a stationary tendency with increase of time. The drag coefficient typically drops rapidly in the very beginning to a minimum value. After that, it increases to a maximum value as the secondary vortices appear and then is slowly down to a constant for $Re = 550$ and 3000. For $Re = 9500$, because the primary vortex begins to detach from the cylinder surface before $t = 2$ and the third vortex is formed in the shear layer at $t \approx 2$, the drag coefficient gradually decreases in a short time and then increases with time. Again, general agreement is good although a little discrepancy was found between the present results and those of Chang and Chern [15] in the middle part of time evolution.

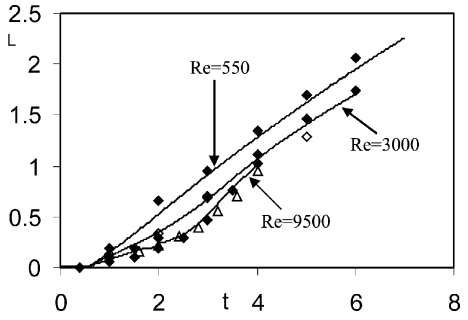

Fig. 17. Time evolution of the wake length for moderate and high Reynolds numbers (experimental data of Bouard and Coutanceau [11]; ◇ and △, results of Loc and Bouard [14] for $Re = 3000$ and 9500 respectively; –, present results).

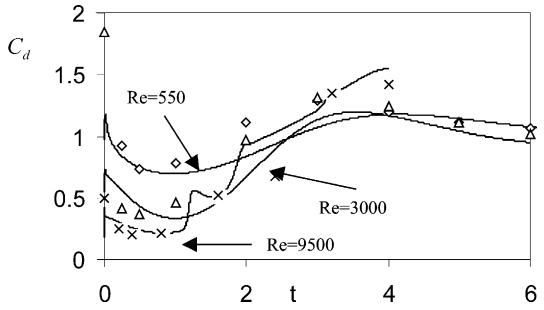

Fig. 18. Time evolution of the drag coefficient for moderate and high Reynolds numbers (symbols are the results of Chang and Chern [15] for $Re = 550$ (◇) 3000 (△) 9500 (×); (–) present results).

5. Conclusions

The explicit Taylor series expansion- and least square-based lattice Boltzmann method is applied in this work to simulate the flow past an impulsively started circular cylinder for Reynolds number range from 20 to 9500. The results of steady state flow at low Reynolds numbers and the early stage of unsteady flow at moderate and high Reynolds numbers were obtained, and compared well with experimental data and numerical results of Navier–Stokes equations available in the literature. In the present simulation, the D2Q7 lattice model and non-uniform meshes were used. From the present work, it was found that our new method is efficient and easy for application to flow problems with curved boundary and non-uniform mesh. In fact, it keeps the local and explicit features of the standard lattice Boltzmann method. No solution of differential equation is involved in the present method.

References

[1] H. Blasius, Z. Angew. Math. Phys. 56 (1908) 1.
[2] S. Goldstein, L. Rosenhead, Proc. Camb. Philos. Soc. 32 (1936) 392.
[3] C.Y. Wang, J. Math. Phys. 46 (1967) 195.
[4] W.M. Collins, S.C.A. Dennis, Q. J. Mech. Appl. Math. 26 (1973) 53.
[5] W.M. Collins, S.C. Dennis, J. Fluid Mech. 60 (1973) 105.
[6] M. Bar-Lev, H.T. Yang, J. Fluid Mech. 72 (1975) 625.
[7] H. Honji, S. Taneda, J. Phys. Soc. Jpn. 27 (1969) 1968.

[8] S. Taneda, Recent Research on unsteady Boundary Layer, vol. 2, Quebec Laval University, 1972.
[9] M. Coutanceau, R. Bouard, J. Fluid Mech. 79 (1977) 231.
[10] M. Coutanceau, R. Bouard, J. Fluid Mech. 79 (1977) 257.
[11] R. Bouard, M. Coutanceau, J. Fluid Mech. 101 (1980) 583.
[12] V.A. Payen, J. Fluid Mech. 4 (1958) 81.
[13] T.P. Loc, J. Fluid Mech. 100 (1980) 111.
[14] T.P. Loc, R. Bouard, J. Fluid Mech. 160 (1985) 93.
[15] C.-C. Chang, R.-L. Chern, J. Fluid Mech. 233 (1991) 243.
[16] P.K. Koumoutsakos, A. Leonard, J. Fluid Mech. 296 (1995) 1.
[17] S. Chen, Z. Wang, X. Shan, G.D. Doolen, J. Statist. Phys. 68 (1992) 379.
[18] L.-S. Luo, Int. J. Mod. Phys. C 8 (1997) P859.
[19] X. He, G.D. Doolen, J. Comp. Phys. 134 (1997) 306.
[20] R. Mei, W. Shyy, J. Comp. Phys. 143 (1998) 426.
[21] Y. Chen, H. Ohashi, M. Akiyama, JSME Int. J. Ser. B 40 (1997) 25.
[22] Q. Zou, X. He, Phys. Fluids 9 (1997) 1591.
[23] G. Peng, H. Xi, C. Duncan, S.H. Chou, Phys. Rev. E 59 (1999) 4675.
[24] M. Su, K. Xu, M.S. Ghidaoui, J. Comp. Phys. 150 (1999) 17.
[25] S. Hou, Q. Zou, S. Chen, G.D. Doolen, G. Cogley, J. Comp. Phys. 118 (1995) 329.
[26] C. Shu, X.D. Niu, Y.T. Chew, Phys. Rev. E. 65 (2002), 036708-13.
[27] L.F. Shampine, Numerical Solution of Ordinary Differential Equations, Chapman & Hall, New York, 1994.
[28] L. James, Buchanan, P.R. Turner, Numerical Methods and Analysis, McGraw-Hill, New York, 1992.
[29] S.C.R. Dennis, G.Z. Chang, J. Fluid Mech. 42 (1970) 471.
[30] B. Fornberg, J. Fluid Mech. 98 (1980) 819.